QA4EO DIMITRI Evolution
Inter-band Vicarious Calibration over Deep Convective Cloud (DCC)

Reference: ARG_DIM_QA4EO_TN_DCC

Version: 1.1

Date: 30th January 2023

	Name	Company/Organization	Signature	Date
Prepared by	Bahjat Alhammoud Cameron Mackenzie	ARGANS Ltd (UK)		20/12/2022
Reviewed by	Nicolas Lamquin	ACRI-ST (FR)		17/01/2023
Reviewed by	Beatrice Berthelot	Magellium (FR)		
Approved by	Marc Bouvet	ESA/ESTEC		

Table of Contents

List of Figures

List of Tables

No table of figures entries found.

Version History

Version	Date	Main changes
0.1	20/12/2022	Creation of this document
1.1	30/01/2023	Addressing reviewers' comments such as clarification on ozone climatology, details on COT retrieval

Reference documents

ID	Reference
RD.1	The Sentinel-2 Radiometric Validation DCC approach – ATBD, SEOM-Project, Ref: S2RadVal-ATBD-001-ACR by N. Lamquin and V. Bruniquel (17/11/2017)

Acronyms

ATBD Algorithm Theoretical Basis Document

COT Cloud Optical Thickness

CPT Cloud Particle Type

DCC Deep Convective Cloud

DU Dobson Unit

EO Earth Observation

ESA European Space Agency.

MSI Multi Spectral Instrument

NIR Near InfraRed

PDF Probability Distribution Function

RAA Relative Azimuth Angle

RTM Radiative Transfer Model

SEOM Scientific Exploitation of Operational Missions

SWIR ShortWave InfraRed

SZA Solar Zenith Angle

TOA Top-Of-Atmosphere

VIS Visible

VNIR Visible and Near InfraRed

VZA Viewing Zenith Angle

Scope of the document

This document describes the Algorithm Theoretical Basis Document (ATBD) for the inter-band radiometric vicarious calibration over Deep Convective Clouds (DCC) approach implemented in DIMITRI in the framework of the ESA contract N°: 400011454/15/I-SBo and its CCN1. This document is the deliverable of the WP 700 of the CCN1.

This document structured as follow:

section 1 is devoted to the introduction and the bibliography of the DCC approach;

section 2 presents the proposed DCC approach;

section 3 describes the the DCC method implementation in DIMITRI;

section 4 presents the radiometric validation results;

section 5 provides the method's uncertainty.

1. Introduction

Deep Convective Clouds are excellent targets for inter-band calibration and long-term absolute calibration monitoring of EO sensors, in the VNIR and SWIR spectral domains. These clouds are very opaque/bright (near Lambertian albedos), very high and large where its vertical extensions can reach the tropical tropopause and stretch over large horizontal distances from the core of the convection to the edges of cirrus anvils (tens up to hundred kilometres). The DCC can be easily detected from space and are recurrent within the tropical belt (±20° latitude). The radiative impact of aerosols and of the ground surface below DCCs is minimal, which simplifies the modelling of the target-to-sensor signal, mainly to reflectivity of the cloud coupled with overlying gaseous absorption.

Vermote and Kaufman (1992, 1995) started to use DCCs to monitor the inter-band calibration of AVHRR VIS and NIR bands. Since then, efforts have been made to characterise and model the variability of DCC reflectance, in order to monitor the trends of calibration gain using different methodologies (e.g. Fougnie and Bach, 2009; Doelling et al. 2011; Steckx et al. 2014; Wang and Cao, 2016; Lamquin et al. 2017 & 2020).

Two distinguished families' approaches use the DCCs. The first is dedicated to inter-band monitoring and relies on the modelling of the DCC reflectance through RTMs (Vermote and Kaufman 1992, 1995; Fougnie and Bach, 2009; Steckx et al. 2014). This technique uses RTMs to simulate the TOA-reflectance over the DCC at the sensor level, more details on this technique provided in the DCC-MAG ATBD (Berthelot 2020).

The second approach relies on a statistical analysis of a large number of DCC observations, coupled with an anisotropy model to correct for cloud BRDF effects, to obtain distributions of the DCC reflectance and quantify invariant indicators (e.g. the mode of the probability distribution function of

the DCC reflectance). This indicator is monitored for trend analysis of the absolute calibration of a sensor (e.g. Doelling et al. 2011; Wang and Cao, 2016). Such indicators can also be fully exploited through comparisons between indicators from similar payloads for cross-calibration purposes (e.g. OLCI-A / OLCI-B cross-calibration in Lamquin et al. 2020).

The DIMITRI DCC-ARG approach implemented here follows this statistical approach developed by Lamquin et al. 2017 in the framework of SEOM contract Ref.: S2RadVal-ATBD-001-ACR detailed below.

1.1. DCC properties

It has been agreed that DCCs can be used as spectral invariant targets to monitor the radiometric response degradation of reflective solar bands of EO sensors (e.g. Chen et al., 2013).

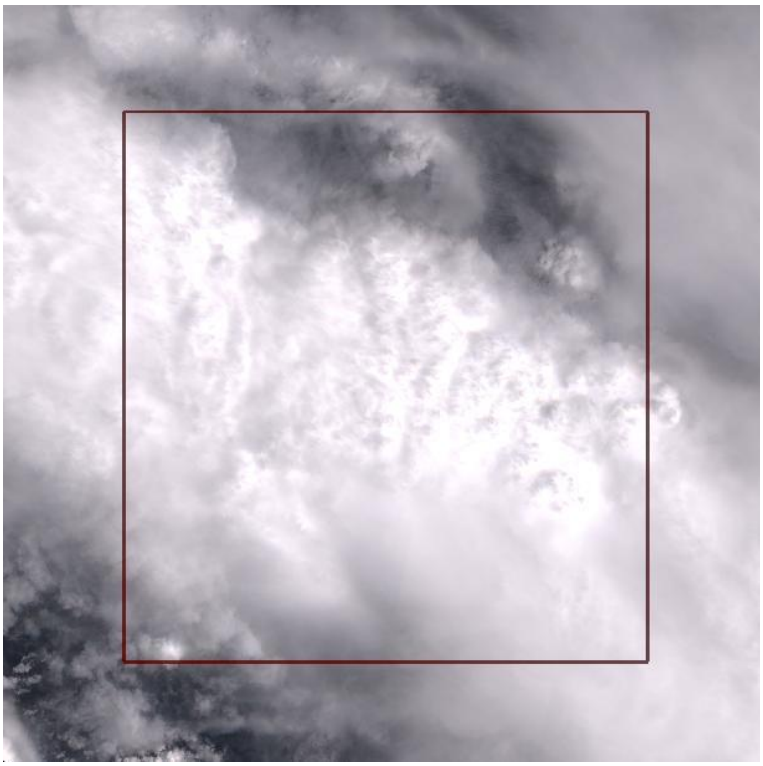

Figure 1. Example of Deep Convective Clouds as observed by MSI (RGB quick-look image over Indonesia: S2A_MSIL1C_20190124T020441_N0207_R017_T51LWG_20190124T061926.SAFE).

1.1.1. DCCs brightness

TOA-reflectance of DCC targets can reach unity in all VIS bands as shown by Fougnie and Bach (2009) from monthly-mean of the TOA-reflectance over POLDER. Using radiative transfer simulations, Chen et al. (2013) confirm that cloud albedo – and later reflectance Probability Distribution Functions (PDF) – tend to stabilize when clouds become optically thick. This is also simulated in Sohn et al. (2009) and reproduced in **Figure 2** for illustration. Moreover, DCCs behave mostly like Lambertian

reflectors, which avoids the use of a bidirectional reflectance distribution function for geometries close to nadir (Sentinel-2/MSI case).

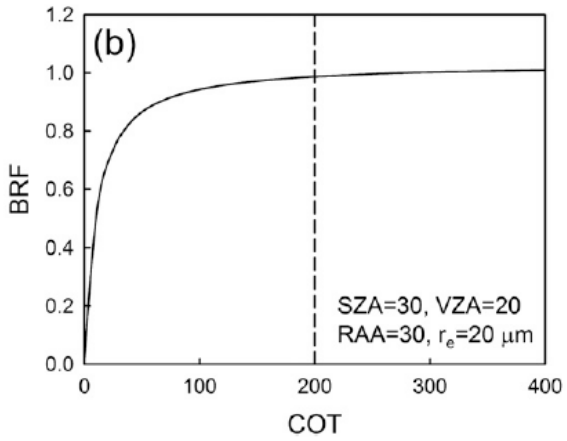

Figure 2. bidirectional reflectance factor evolution with cloud optical thickness on DCC RTM simulations. From Sohn et al. (2009).

1.1.2. DCCs extent

DCCs have large vertical extent stretching from the near surface up to the tropopause region (about 16–18 km in the Tropics), their tops are therefore very cold (about 200 K). Their horizontal spread depends on the size and level of maturity of their generator convective system (e.g. Futyan & Del Genio, 2007) so that DCCs appear over horizontal scales from few to hundreds of kilometers.

The tropopause, where the temperature gradient inverts, behaves as a physical barrier to the progression of the strong upward convection generating DCCs. For this reason, DCCs top height is generally found in relationship with the tropopause (Pan and Munchak, 2011).

They are made of water droplets on about their lower half and ice particles on their upper part. They are also very dense clouds and consequently exhibit very-high optical depths (order-of-magnitude 100), which minimizes the contributions of molecular scattering, aerosols, and ground to the TOA signal, at the exception of strong stratospheric aerosol loadings from volcano eruptions.

2. Overview of the proposed DCC approach

The DCC radiometric calibration method is based on the observation of Deep Convective Clouds. It is considered as an "inter-band" validation approach. It allows the validation of the radiometry in one band relatively to another one considered as accurately calibrated. The DCC method is complementary to the well-known absolute Rayleigh method extending the validation beyond the red to the NIR.

2.1. Principle of the DCC approach

It has been agreed that DCCs can be used as spectral invariant targets to monitor the radiometric response. Hence the current DIMITRI's DCC-ARG method has been implemented following the **DCC approach defined in the frame of the "Sentinel-2 Radiometric Validation" study of the Scientific Exploitation of Operational Missions (SEOM) programme [RD.1].**

2.1.1. DCC Pixels selection

Absorption from water vapor at 1375 nm is the determining criterion for the selection of DCC pixels within Sentinel-2 images: pixels are selected if their TOA reflectance at 1375 nm is above a threshold of 0.4 and its extent is higher than 20 % of the total pixels number. In addition, the pixels with TOA reflectance at 945 nm should be above a threshold of 0.4 and its extent is higher than 70%. Then all pixels with TOA reflectance at 865 nm higher than 0.7 are selected.

Selection according to geometry to avoid strong off-zenith illuminations and/or strong off-nadir observations is performed though not necessary as deep convection is concomitant with high solar zenith angles (lower than 40°) and MSI acquisitions are very close to nadir (lower than 15°) [Lamquin et al. 2017].

In order to increase the DCC samples and to get smoother intra-DCC spatial variability, the selected pixels are clustered within the ROI, where small clusters <10 km (radius) are rejected. To minimise the radiometric spatial noise the valid pixels are agglomerated into macropixels (n x n pixels user defined; default value for Sentinel-2/MSI n=100 ⇔ 6 km).

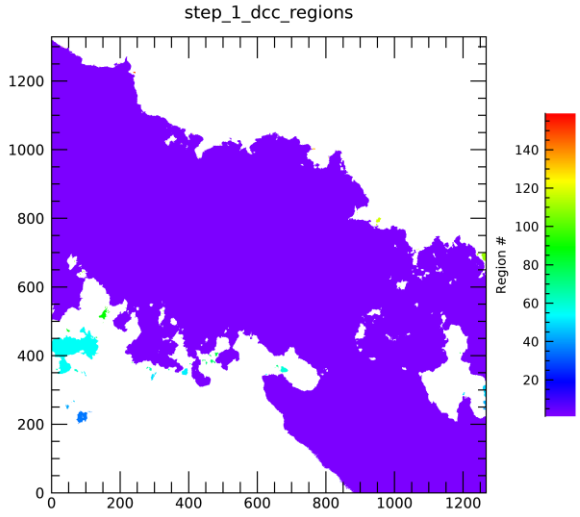

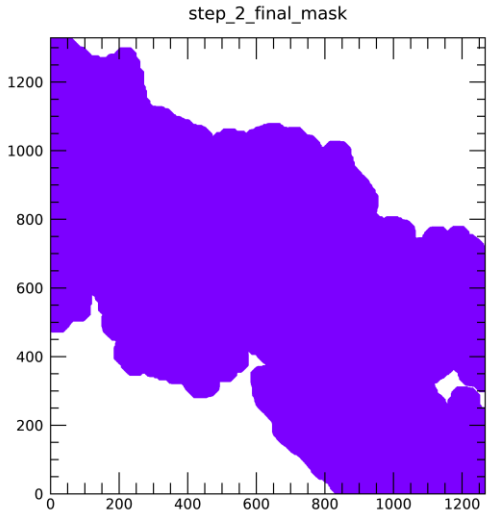

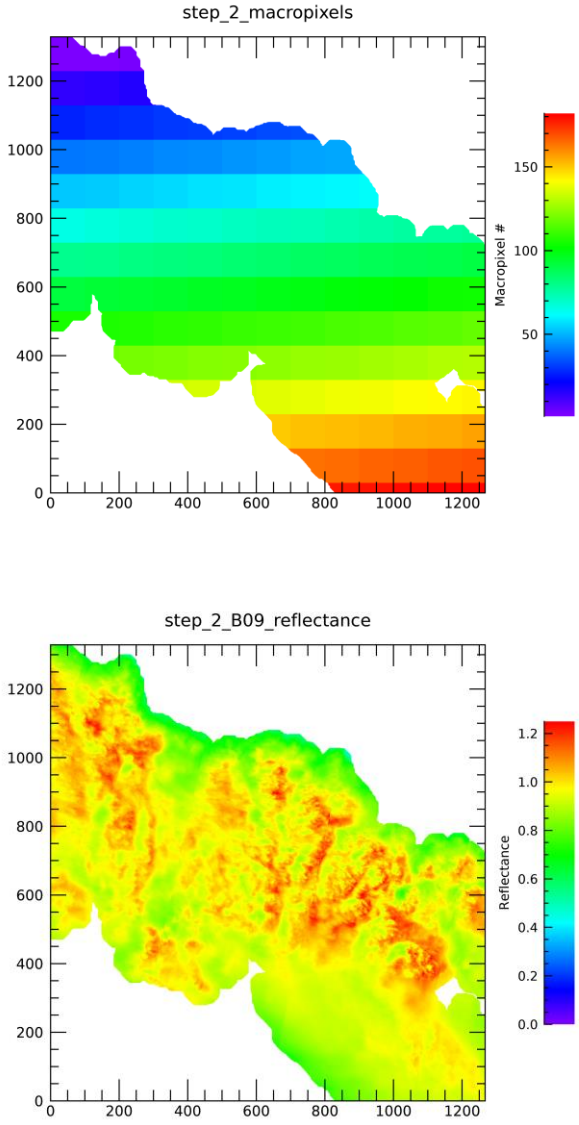

Figure 3. (Top to bottom): DCC clusters, final selection mask, macro-pixels (100 x 100 pixels) and B09 (865 nm) TOA-reflectance respectively over the ROI from S2A/MSI image in **Figure 1**.

2.1.2. Statistics computation and data storage

After the selection of DCC pixels, statistics of the MSI radiometry and of the other necessary parameters (geometry of acquisition, ozone content, etc.) is performed for each block of pixels. The median of TOA reflectance is taken for each wavelength to represent the TOA reflectance for each micropixel to be used as input of the methodology.

2.1.3. DCC TOA reflectance simulation

2.1.3.1. DCC TOA reflectance modelling

In fact, the signal of the observed DCC TOA at the sensor level can be expressed as the sum of two main contributions from the atmosphere and DCC, weighted by the stratospheric gaseous transmission (equation 1).

$$\rho_{TOA}(\theta_s,\theta_v,\Delta\varphi,\lambda) = (\rho_{atm}(\theta_s,\theta_v,\Delta\varphi,\lambda) + \rho_{DCC}(\theta_s,\theta_v,\Delta\varphi,\lambda)).T_{gas}(\theta_s,\theta_v,\lambda) \quad (1)$$

Where:

$\rho_{atm}(\theta_s,\theta_v,\Delta\varphi,\lambda)$ is the atmospheric signal (essentially Rayleigh scattering) from the layers above and within the cloud;

$\rho_{DCC}(\theta_s,\theta_v,\Delta\varphi,\lambda)$ is the reflectance at the top of the cloud resulting in the interactions of light with the cloud;

$T_{gas}(\theta_s,\theta_v,\lambda)$ is the stratospheric gaseous transmission.

The following assumptions are considered:

- the signal coming from the surface below the cloud, and which is particularly dark compared to the cloud reflectance, can be neglected.
- the signal coming from the atmosphere only corresponds to the molecular scattering and absorption.
- the signal coming from the aerosols above the clouds has a negligible impact. Indeed, aerosols are mainly distributed at lower altitude (except in exceptional cases of stratospheric volcanic ashes).
- scattering within the cloud and absorption by stratospheric trace gases are physically decoupled. The computation domain can be split into two domains delimited by the cloud top (which proxy is the tropopause): one purely absorbing domain containing the effective trace gases such as ozone and water vapour, the other (within the cloud) nearly purely diffusive in the VIS containing ice particles. Stratospheric gaseous transmission is applied on the signal coming from the atmosphere and the DCC.

2.1.3.2. Standard atmospheric profiles

Standard atmospheric profiles are taken from McClatchey et al. (1972) with the following assumptions:

- Air concentration is fix and very stable with latitude.
- Water vapour concentration only provides variation below 12 km with fixed profile.
- Ozone has the major effect on stratospheric gaseous absorption with maximum concentration in the stratosphere. Its concentration exhibits a peak altitude shift with latitude which corroborates the tropopause shift (high tropopause in the Tropics, low at the poles). Ozone concentration drastically increases from about the tropopause region (15-20 km in the Tropics) upwards. Its regional and seasonal variability, plus its vertical

distribution variability induced by the altitude of the tropopause, have to be taken into account with best accuracy.

- Ozone content is taken from auxiliary climatology of the ESA project Ozone Climate Change Initiative (CCI) (www.esa-ozone-cci.org) or OzoneCCI. Thie climatology show a typical seasonal variability of the ozone content between 230 and 300 Dobson units (**Figure 4** and **Figure 5**). These values are taken into account for the LUTs computing.

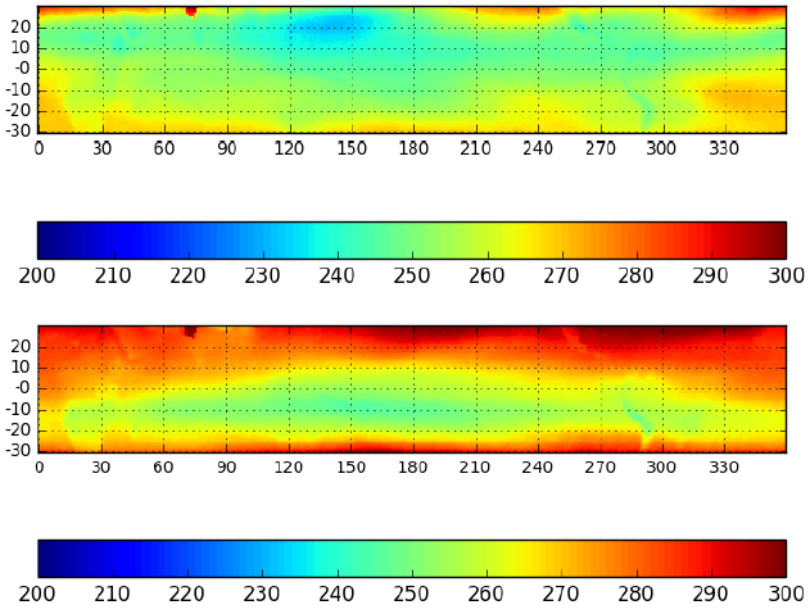

Figure 4. Monthly mean total column ozone concentration in DU (January top, July bottom). From OzoneCCI monthly data products [RD1].

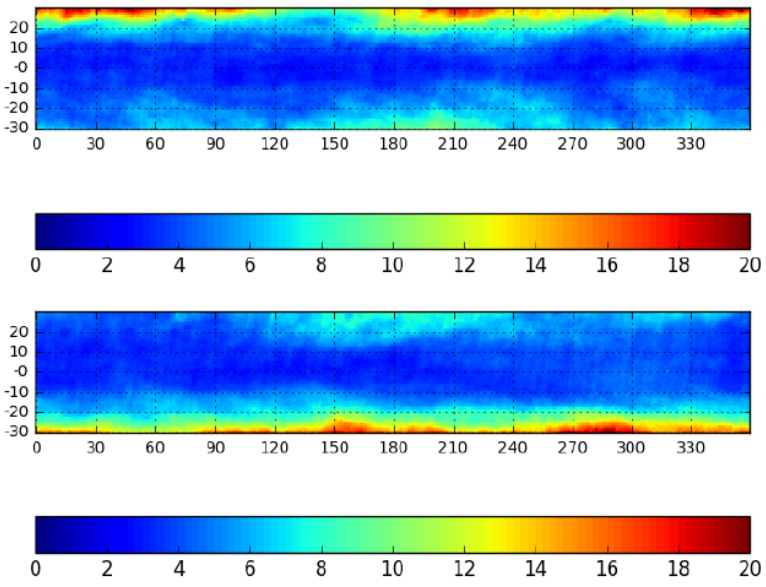

Figure 5. Standard deviation of monthly mean total column ozone concentration in DU (January top, July bottom). From OzoneCCI monthly data products [RD1].

2.1.3.3. Stratospheric gas absorption

Note that above DCCs, gas absorption, which effect is to decrease gaseous transmittance $T_{gas}(\theta_s,\theta_v,\lambda)$, has main contributions from water vapour, ozone, oxygen, and NO2 in the VIS. Hence the stratospheric gaseous transmission is computed as follows:

$$T_{gas}(\theta_s, \theta_v, \lambda) = T_{gas}(0, 0, \lambda)^{a/2} \qquad (2)$$

$$a = 1/\cos\theta_s + 1/\cos\theta_v \qquad (3)$$

$T_{gas}(0, 0, \lambda)$ is a two-way transmittance in nadir/zenith configuration

Sensitivity of nadir transmittance with respect to the tropopause altitude is shown in **Figure 6** for a fixed ozone total-column concentration of 250 DU over the useful MSI spectrum (up to B10). Transmission is modified in the water vapour and oxygen absorption bands. Only B9 and B10 (water vapour absorption bands indeed) are strongly impacted (other bands carefully avoiding the absorbing features or only experiencing slight absorption).

Sensitivity of nadir transmittance with respect to ozone total-column concentration is shown in **Figure 6** for a fixed tropopause altitude of 16 km over the useful MSI spectrum (up to B10). Transmission is mainly modified in the Chappuis ozone absorption continuum, which is impacting all bands in the VNIR and especially B2 (490 nm), B3 (560 nm) and B4 (665 nm).

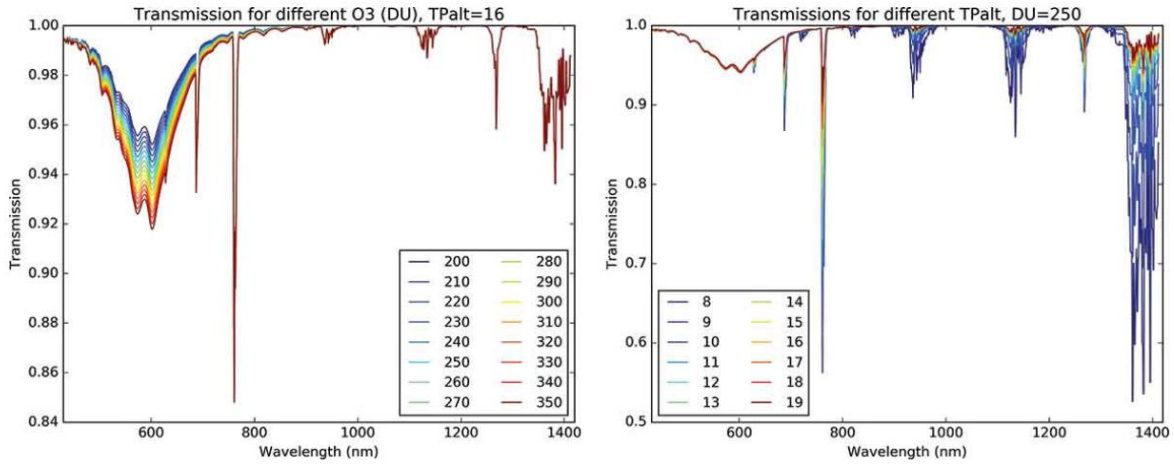

Figure 6. Above-DCC transmission for tropopause at 16 km and total-column ozone content from 200 to 350 DU (left) and for ozone content of 250 DU and tropopause altitude from 8 to 19 km (right). Wavebands between 430 and 1412 nm (Lamquin et al. 2018).

2.1.3.4. DCC macro/micro-physics

A mean macrophysical DCC is modelled as a cloud extending from near the surface (i.e. 1 km) to the tropopause. The lowest half of it is modelled as water droplets, the other top half as ice. Two alternative models are used considering a 1/3 or a 2/3 vertical division of water and ice.

Without any possibility to directly assess the cloud top altitude, the tropopause altitude is used as a proxy. This one is provided by a climatology (here from NOAA, see D.2).

The optical properties of the DCC are defined by:

- the Cloud Optical Thickness (COT) which is retrieved from a reference band (see below)
- the particle size, which is assumed fixed for a given retrieval, will be given representative values (see below)

Ice crystals microphysics is considered by means of the Baum et al. (2005) bulk scattering parameterization. It consists in phase functions and other parameters representative of a mean distribution of ice crystals within cirrus clouds. It is discretized per wavelength every 10 microns and per particle effective diameter every 10 microns.

2.1.3.5. Radiative transfer modelling, and LUTs computation

The ARTDECO (Atmospheric Radiative Transfer Database for Earth and Climate Observation) framework (http://www.icare.univ-lille1.fr/projects/artdeco) has been chosen for the simulation of the DCC TOA reflectance and the LUTs generation [RD-1] for further details.

The working hypothesis is that stratospheric absorption and tropospheric reflectance (DCC and atmosphere) are decoupled. Each term is then simulated separately and sampled in separate LUTs [RD.1].

To carry all possible atmospheric states, nadir transmittances are computed for:

- ozone total-column content between 200 and 350 by steps of 10 DU
- tropopause altitude between 8 and 19 by steps of 1 km
- all MSI bands between 443 and 1375 nm

2.1.3.6. DCC TOA reflectance computation

Finally $\rho_{atm}(\theta_s,\theta_v,\Delta\varphi,\lambda_{\mathrm{MSI}})$ & $\rho_{DCC}(\theta_s,\theta_v,\Delta\varphi,\lambda_{\mathrm{MSI}})$ are simulated for various COT and ice crystal effective diameters (De). Ranges are taken from the results of Sohn et al. (2015). The full dependencies then account for:

- COT between 40 and 200 by step of 20;
- De between 40 and 80 microns by step of 10 microns;

- θs between 0° and 60° by step of 2.5°;
- θv between 0° and 15° by step of 2.5°;
- $\Delta\varphi$ between 0° and 180° by step of 2.5°;
- all nominal MSI wavelengths between 443 and 1375 nm.

The dependency with COT (at fixed De) shows a strong monotonous response in all wavebands whereas the dependency with De (at fixed COT) is only strongly effective in the SWIR (1375 nm) **Figure 7**. Through the interband methodology there is no way to guide the retrieval by assessing precisely the ice crystal effective diameter; we only possess a rough range of the values. Interestingly, an increase of De provides a slight increase of the simulated spectral slope. We therefore use De as a fixed parameter for independent assessments of the gains because its uncertainty is more likely to provide bias in the final results.

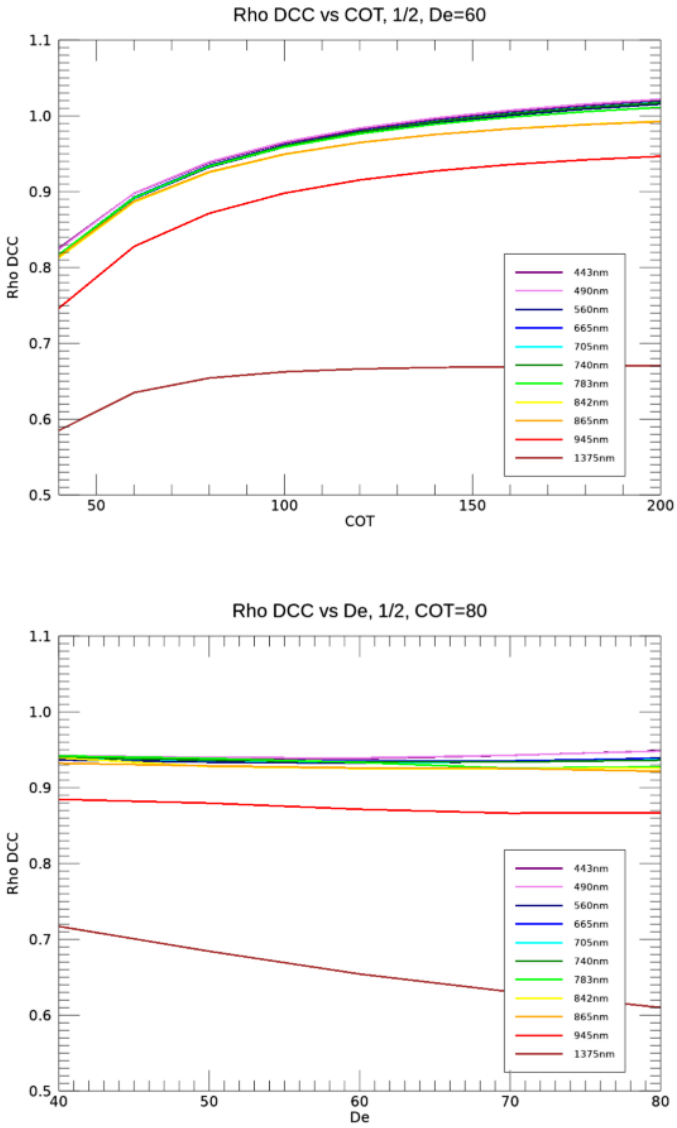

Figure 7. Tropospheric reflectance dependency with COT (top) and De (bottom) when other parameter fixed (resp. De=60 microns, COT=80). Geometry case SZA=20°, VZA=10°, RAA=20°.

2.1.3.7. Retrieval of the DCC COT at a reference wavelength

The Cloud Optical Thickness (COT) is retrieved at reference wavelength (λ_{ref}) by comparing the MSI reflectance corrected for transmittance computed in the conditions of observations $\rho^{\mathrm{t}}{}_{MSI}(\lambda_{ref})$ to the simulated tropospheric reflectance $\rho^{\mathrm{t}}{}_{\mathrm{RTM}}(\lambda_{ref},\ COT)$ from the RTM LUTs. This is done by fitting a polynomial relationship $P^{\lambda_{\mathrm{ref}}}_{\rho\rightarrow\mathrm{COT}}$ between *log(COT)* and $\rho^{\mathrm{t}}{}_{\mathrm{RTM}}(\lambda_{ref})$.

$$\log(COT) = P^{\lambda_{ref}}_{\rho\rightarrow COT}(\rho) \quad (4)$$

Then the DCC COT is retrieved by taking the value at $\rho^{t}{}_{MSI}(\lambda_{ref})$

$$\log(COT_{MSI}) = P^{\lambda_{ref}}_{\rho \to COT}(\rho^{t}_{MSI}(\lambda_{ref})) \quad (5)$$

Then the retrieved DCC COT propagated to the other bands

$$\rho^{t}_{RTM}(\lambda) = P^{\lambda}_{COT \to \rho}(\log(COT_{MSI})) \quad (6)$$

various COT and ice crystal effective diameters (De). Ranges are taken from the results of Sohn et al. (2015). The full dependencies then account for:

3. DCC Implementation in DIMITRI

The DCC-ARG calibration methodology is implemented as an individual IDL module, called by a setup GUI module (or directly in command line); it then calls several separated routines for specific jobs (e.g. check suitability, create macropixels, computation of DCC reflectance, etc.).

Schematically, the main DCC-ARG calibration module are (**Figure 8**):

- Interfaces with the DIMITRI database to identify appropriate L1b extractions with respect to chosen region, sensor, processing version and year;
- Screens data for ROI cloud and region coverage pixel-by-pixel;
- Finds all pixels within other user defined parameters specific to the calibration method;
- Reads all RTM LUTs;
- Performs the DCC calibration band per band;
- Post-processed the coefficients (averaged, statistics);
- Outputs the individual and averaged calibration coefficients for each band in several netcdf and image files.

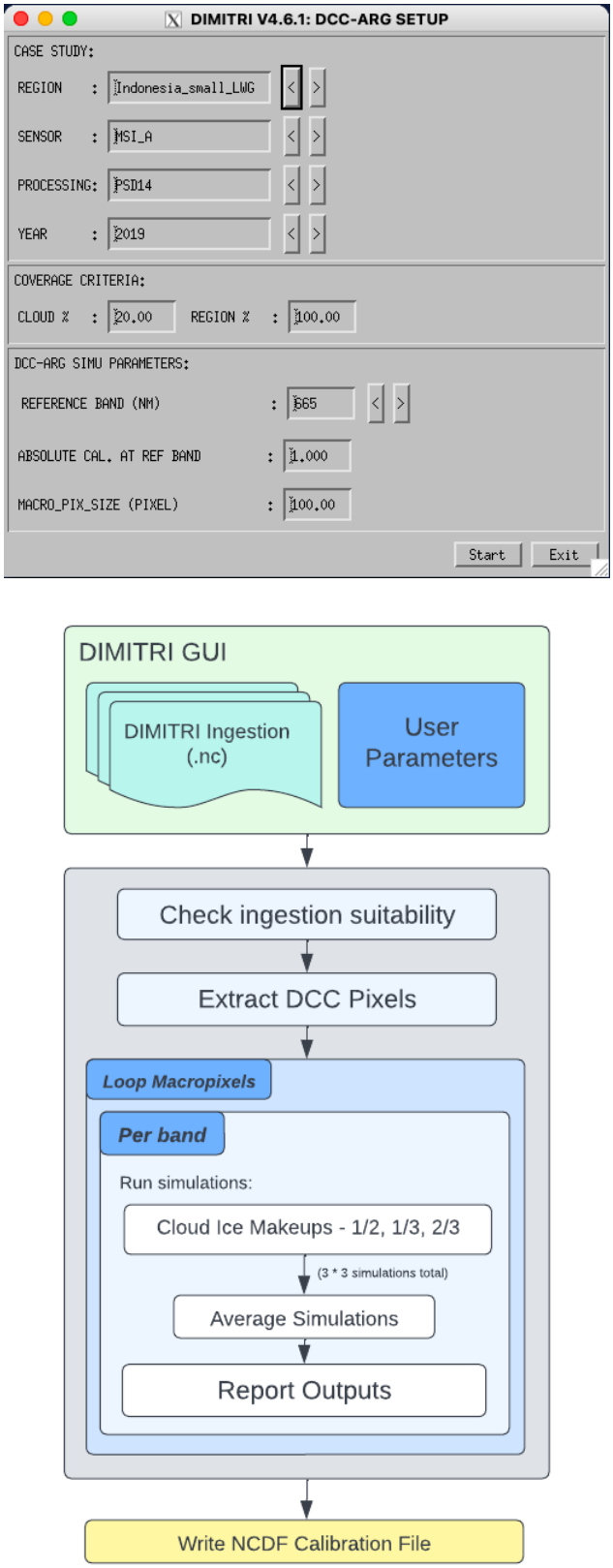

Figure 8. DCC-ARG setup GUI (top) and processing flowchart (bottom).

4. Results of the DCC Implementation in DIMITRI

The DCC method provides the ratios between simulated and measured TOA reflectances for individual inter-band calibration gains per DCC target (**Figure 9** and **Figure 10**). Writing $g(\lambda)_i$, where i stands for the target per cloud makeup (1/2, 1/3, 2/3), we have:

$$g(\lambda)i = \rho_{MSI}(\lambda)i/\rho_{RTM}(\lambda)i$$

By definition $g(\lambda_{\text{ref}})i = 1$.

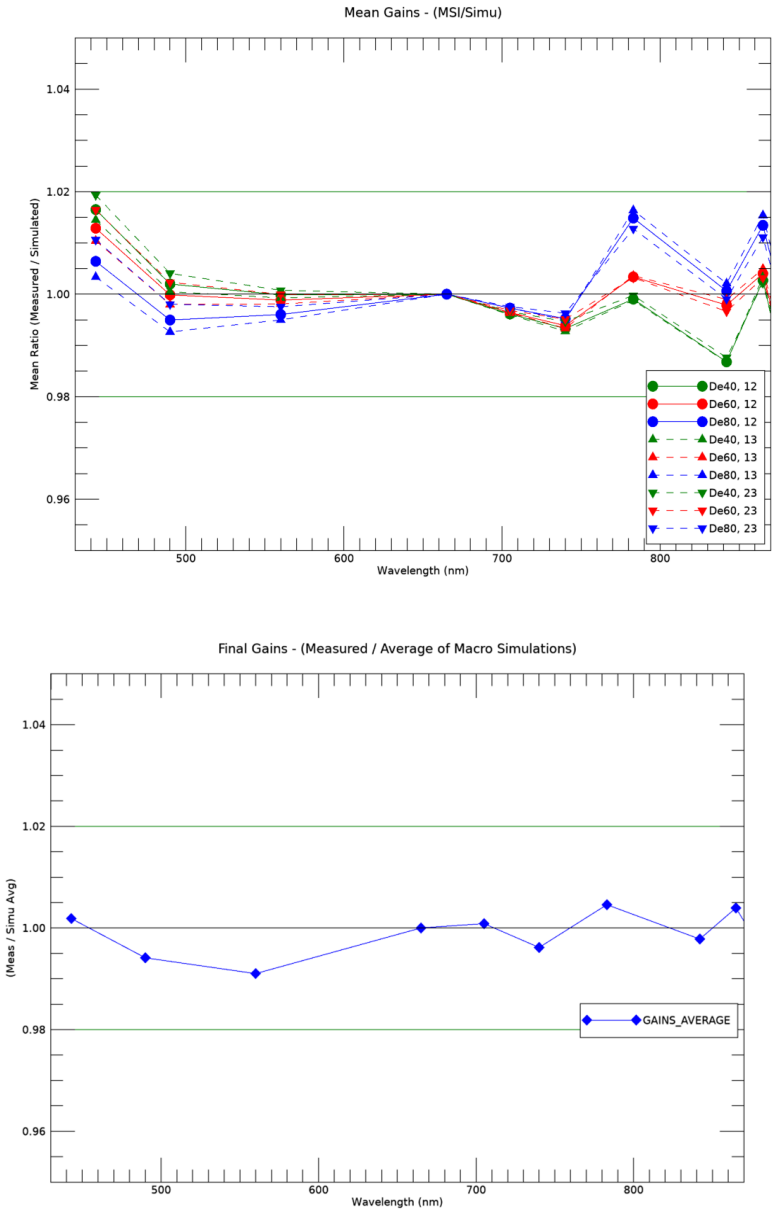

Figure 9. DCC-ARG gains coefficients per cloud-makeup (top) and average (bottom).

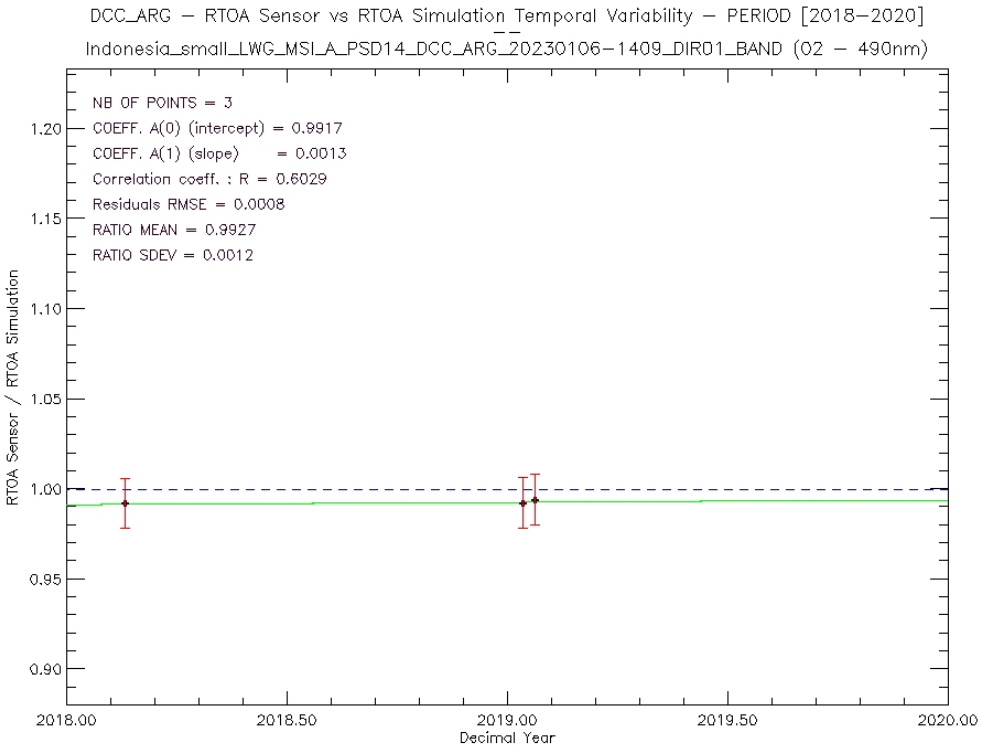

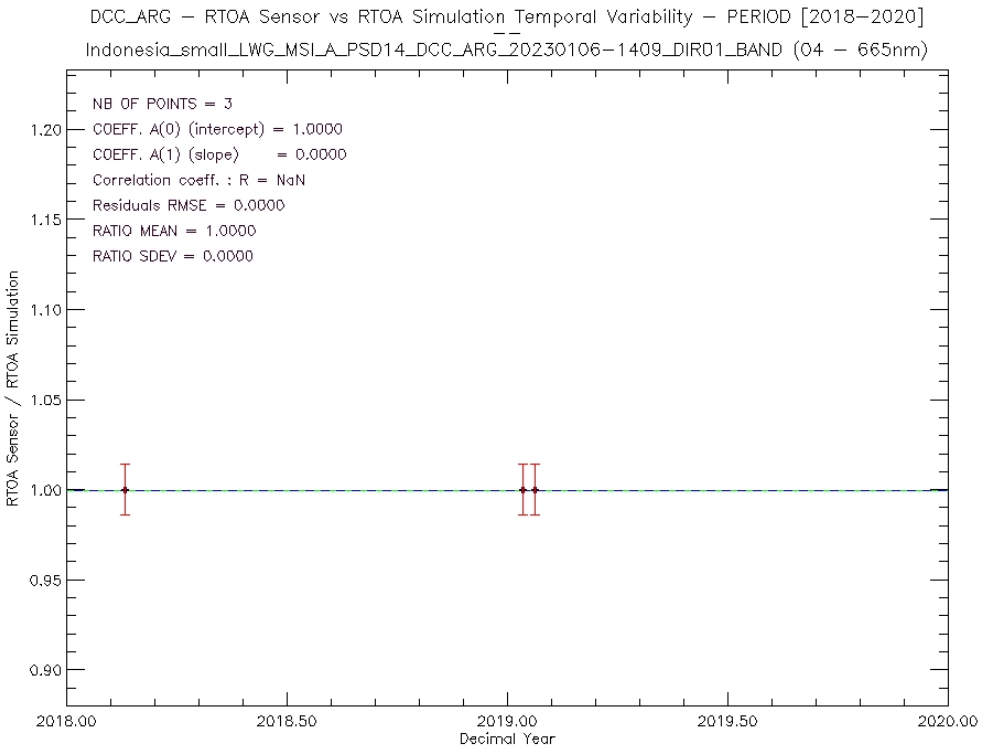

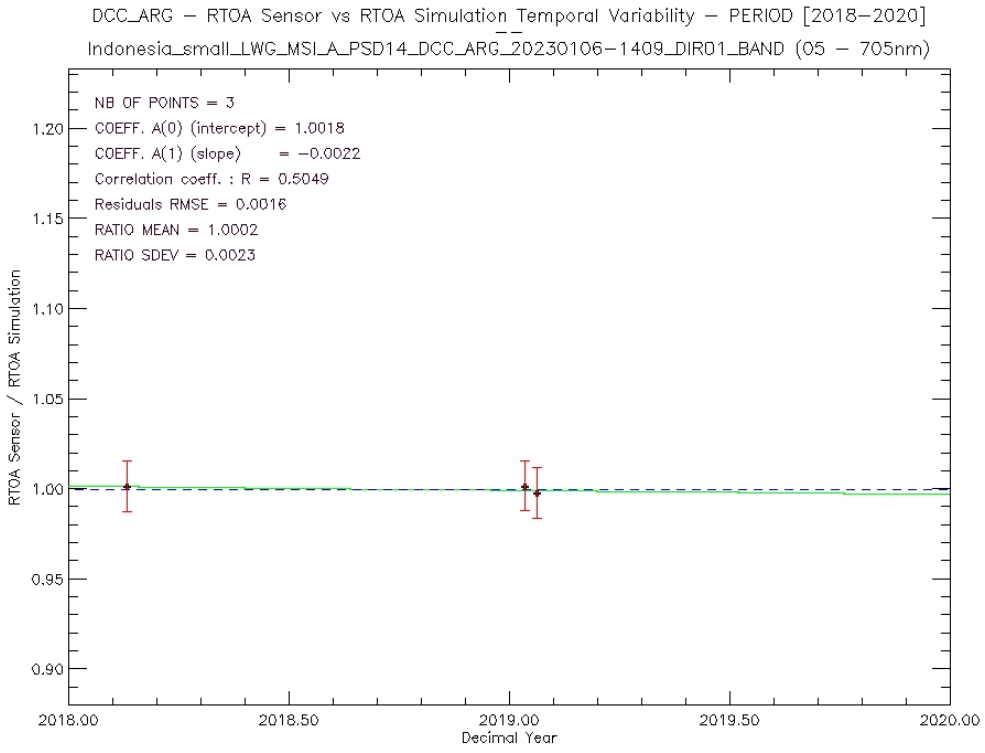

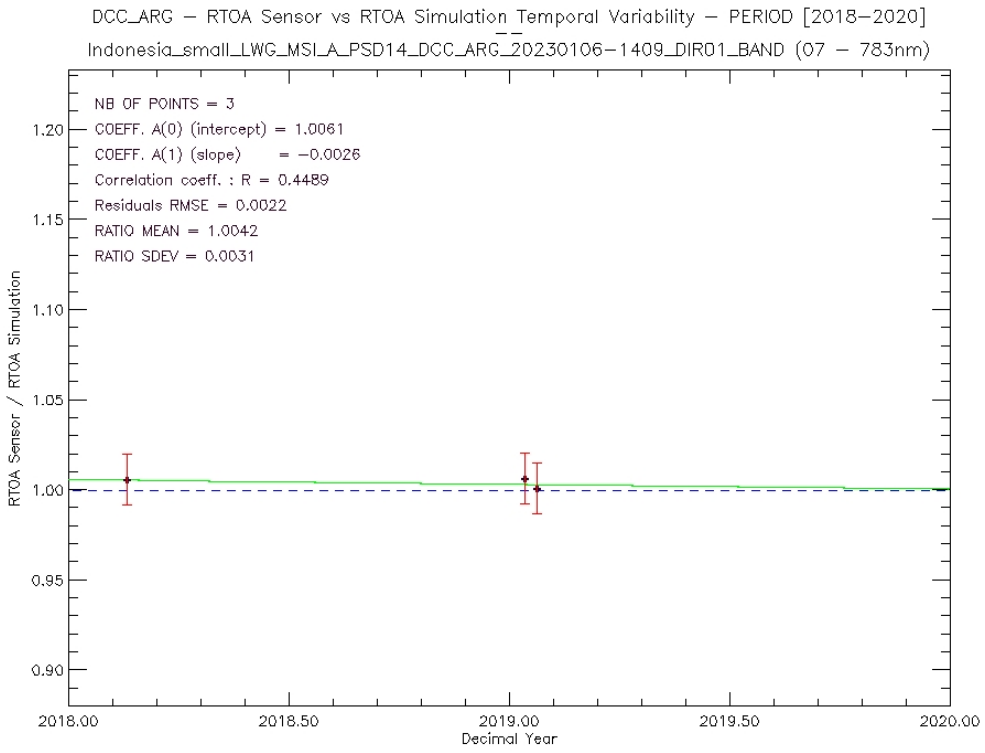

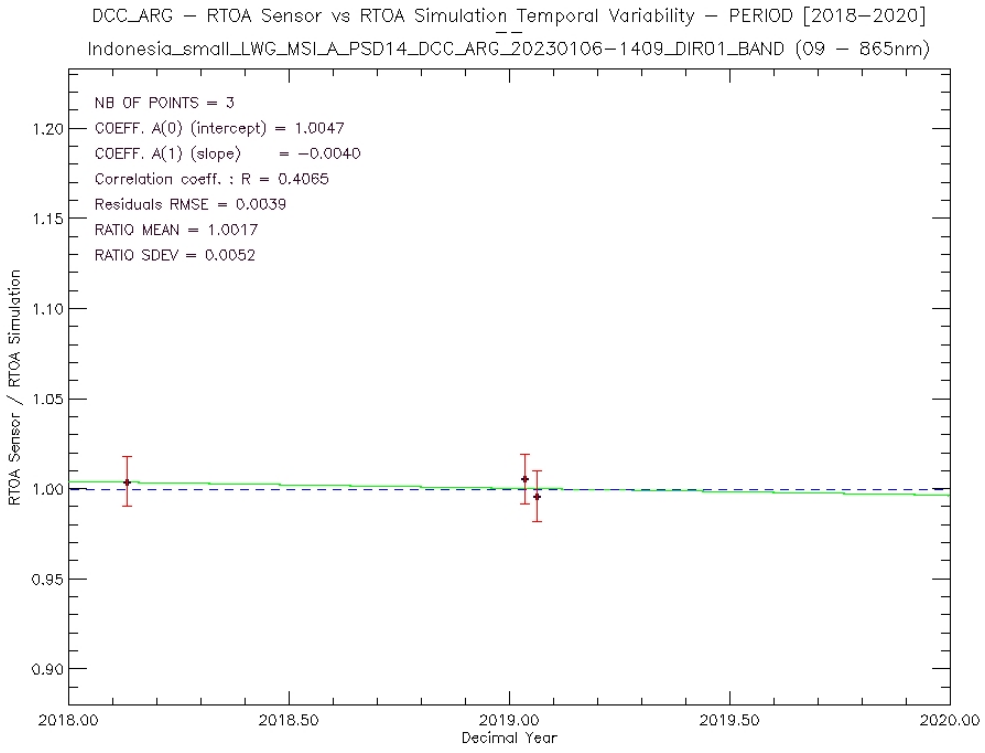

Figure 10. time-series of DCC-ARG gain-coefficients per band (top to bottom) bands 490, 665 (ref), 705, 783, 865 nm from MSI-A over Indonesia site.

5. the DCC method's uncertainty

The DCC method uncertainty budget at individual gain level has been adopted from Lamquin et al. 2018 and presented below on **Figure 11**

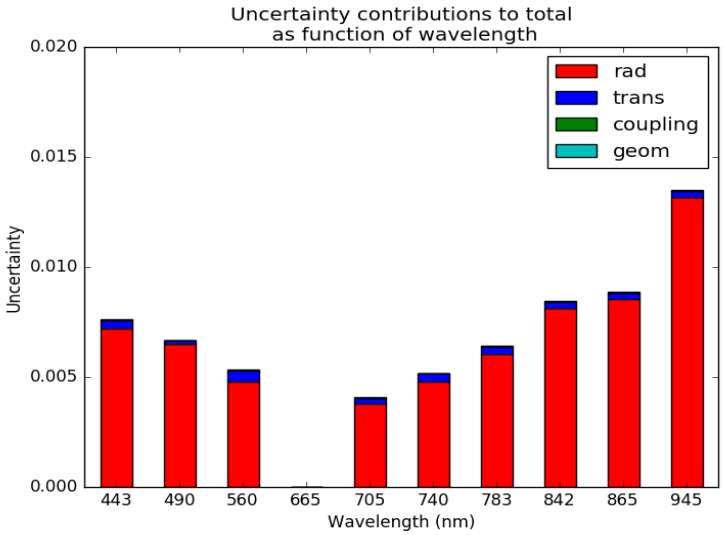

Figure 11. Total uncertainty budget (expressed as standard deviation) from an MSI image [RD1]

References

BERTHELOT 2020, RFQ-QA4EO-DIMITRI-TN-010-MAG_ATBD-DCC-V1.4.

CHEN, L., HU, X., XU, N., & ZHANG, P. (2013). THE APPLICATION OF DEEP CONVECTIVE CLOUDS IN THE CALIBRATION AND RESPONSE MONITORING OF THE REFLECTIVE SOLAR BANDS OF FY-3A/MERSI (MEDIUM RESOLUTION SPECTRAL IMAGER). REMOTE SENSING, 5(12), 6958–6975. DOI:10.3390/RS5126958

DOELLING, D.R.; HONG, G.; MORSTAD, D.L.; BHATT, R.; GOPALAN, A.; XIONG, X. THE CHARACTERIZATION OF DEEP CONVECTIVE CLOUD ALBEDO AS A CALIBRATION TARGET USING MODIS REFLECTANCES. PROC. SPIE 2010, DOI:10.1117/12.869577

FOUGNIE, B., & BACH, R. (2009). MONITORING OF RADIOMETRIC SENSITIVITY CHANGES OF SPACE SENSORS USING DEEP CONVECTIVE CLOUDS: OPERATIONAL APPLICATION TO PARASOL. IEEE TRANSACTIONS ON GEOSCIENCE AND REMOTE SENSING, 47, 851–861. DOI:10.1109/TGRS.2008.2005634

GASCON, F., BOUZINAC, C., THÉPAUT, O., JUNG, M., FRANCESCONI, B., LOUIS, J., ... FERNANDEZ, V. (2017). COPERNICUS SENTINEL-2A CALIBRATION AND PRODUCTS VALIDATION STATUS. REMOTE SENSING, 9, 584. DOI:10.3390/RS9060584

LAMQUIN N., V. BRUNIQUEL & F. GASCON (2018) SENTINEL-2 L1C RADIOMETRIC VALIDATION USING DEEP CONVECTIVE CLOUDS OBSERVATIONS, EUROPEAN JOURNAL OF REMOTE SENSING, 51:1, 11-27, DOI: 10.1080/22797254.2017.1395713

LAMQUIN ET AL., 2020, OLCI A/B TANDEM PHASE ANALYSIS, PART 3: POST-TANDEM MONITORING OF CROSS-CALIBRATION FROM STATISTICS OF DEEP CONVECTIVE CLOUDS OBSERVATIONS, REMOTE SENSING.

MCCLATCHEY, R.A., FENN, R.W., SELBY, J.E.A., VOLZ, F.E., & GARING, J.S. (1972). OPTICAL PROPERTIES OF THE ATMOSPHERE. AIR FORCE CAMBRIDGE RESEARCH LABORATORY, ENVIRONMENTAL RESEARCH PAPER, 411, 3RD ED., BEDFORD, MA. 110.

SOHN, B.J., CHOI, M.J., & RYU, J. (2015). EXPLAINING DARKER DEEP CONVECTIVE CLOUDS OVER THE WESTERN PACIFIC THAN OVER TROPICAL CONTINENTAL CONVECTIVE REGIONS. ATMOSPHERIC MEASUREMENT TECHNIQUES, 8, 4573–4585. DOI:10.5194/AMT-8-4573-2015

STERCKX ET AL. 2014, THE PROBA-V MISSION: IMAGE PROCESSING AND CALIBRATION, INTERNATIONAL JOURNAL OF REMOTE SENSING, 35:7, 2565-2588, DOI: 10.1080/01431161.2014.883094 ;

VERMOTE E.F. AND Y. J. KAUFMAN, "ABSOLUTE CALIBRATION OF AVHRR VISIBLE AND NEAR INFRARED CHANNELS USING OCEAN AND CLOUD VIEWS," INT. J. REMOTE SENS., VOL. 16, NO. 13, PP. 2317–2340, 1995.

WANG, W., & CAO, C. (2016). MONITORING THE NOAA OPERATIONAL VIIRS RSB AND DNB CALIBRATION STABILITY USING MONTHLY AND SEMI-MONTHLY DEEP CONVECTIVE CLOUDS TIME SERIES. REMOTE SENSING, 8, 32. DOI:10.3390/RS8010032

End Of Document